CrossMark

Improving the Automated Coronal Jet Identification with U-NET

Jiajia Liu (刘佳佳)[1,2] ⓘ, Chunyu Ji (季春瑜)[2] ⓘ, Yimin Wang (王宜敏)[3] ⓘ, Szabolcs Soós[4,5] ⓘ, Ye Jiang (姜也)[6] ⓘ,
Robertus Erdélyi[4,5,7] ⓘ, M. B. Korsós[4,5,8] ⓘ, and Yuming Wang (汪毓明)[1,2] ⓘ

[1] Deep Space Exploration Lab/School of Earth and Space Sciences, University of Science and Technology of China, Hefei, 230026, People's Republic of China;
jiajialiu@ustc.edu.cn
[2] CAS Key Laboratory of Geospace Environment/CAS Center for Excellence in Comparative Planetology/Mengcheng National Geophysical Observatory,
University of Science and Technology of China, Hefei, 230026, People's Republic of China
[3] School of Data Science, Qingdao University of Science and Technology, Qingdao, 266100, People's Republic of China
[4] Department of Astronomy, Eötvös Loránd University, Budapest, Pázmány P. sétány 1/A, H-1117, Hungary
[5] Gyula Bay Zoltán Solar Observatory (GSO), Hungarian Solar Physics Foundation (HSPF), Petőfi tér 3., Gyula, H-5700, Hungary
[6] School of Information Science and Technology, Qingdao University of Science and Technology, Qingdao, 266100, People's Republic of China
[7] Solar Physics and Space Plasma Research Centre (SP2RC), School of Mathematics and Statistics, The University of Sheffield, Sheffield, S3 7RH, UK
[8] University of Sheffield, Department of Automatic Control and Systems Engineering, Amy Johnson Building, Portabello Street, Sheffield, S1 3JD, UK
Received 2024 January 24; revised 2024 July 9; accepted 2024 July 21; published 2024 September 9

Abstract

Coronal jets are one of the most common eruptive activities in the solar atmosphere. They are related to rich physics processes, including, but not limited to, magnetic reconnection, flaring, instabilities, and plasma heating. Automated identification of off-limb coronal jets has been difficult due to their abundant nature, complex appearance, and relatively small size compared to other features in the corona. In this paper, we present an automated jet identification algorithm (AJIA) that utilizes true and fake jets previously detected by a laborious semiautomated jet detection algorithm (SAJIA) as the input of an image segmentation neural network U-NET. It is found that AJIA can achieve a much higher (0.81) detecting precision than SAJIA (0.34) while giving the possibility of whether each pixel in an input image belongs to a jet. We demonstrate that with the aid of artificial neural networks, AJIA can enable fast, accurate, and real-time off-limb coronal jet identification from Solar Dynamics Observatory/Atmospheric Imaging Assembly 304 Å observations, which are essential in studying the collective and long-term behavior of coronal jets and their relation to the solar activity cycles.

Unified Astronomy Thesaurus concepts: Solar activity (1475); Plasma jets (1263); Neural networks (1933); Observational astronomy (1145); Astronomy image processing (2306); Solar cycle (1487)

1. Introduction

Jets are abundant in the solar atmosphere. A large amount of jets with various scales and temperatures originating from different locations on disk or off limb have been observed using modern telescopes since the first observations of Hα surges ("cold jets"; Newton 1934) almost one century ago. Based on their different sizes, solar jets are often divided into two categories: small-scale jets and large-scale jets.

Small-scale jets are usually referred to as spicules. Spicules are further subdivided into the traditional Secchi type (also called as type I) and the ones generated by magnetic reconnections (type II, which is also referred to as rapid blue/red excursions), while both are usually observed in the chromosphere and transition region (e.g., Beckers 1968; Sterling 2000; De Pontieu et al. 2007; Sekse et al. 2012). The importance of small-scale jets is well known as they are suggested to have substantial contributions to coronal heating and solar wind acceleration (e.g., He et al. 2009; Moore et al. 2011; Goodman 2012; Samanta et al. 2019). The triggering mechanisms of spicules are complicated, which could involve (combined) effects of small-scale magnetic reconnections (e.g., De Pontieu et al. 2007; Samanta et al. 2019), waves (e.g., Heggland et al. 2007; Jess et al. 2009, 2012; Dey & Chatterjee 2022), and vortices/Alfvén pulses (e.g., Liu et al. 2019a, 2019b; Oxley et al. 2020; Battaglia et al. 2021; Scalisi et al. 2021b, 2021a).

Large-scale jets have been given different names based on the passbands they are observed in, including white-light jets (e.g., Filippov et al. 2011; Kudriavtseva & Prosovetsky 2019), Hα surges (e.g., Brooks et al. 2007; Zhelyazkov et al. 2015), UV/EUV jets (e.g., Liu et al. 2015a; Chen et al. 2017; Liu et al. 2019c; Zhang et al. 2021; Schmieder et al. 2022), and X-ray jets (e.g., Shibata et al. 1992; Cirtain et al. 2007). Although various models have been proposed (e.g., Shibata et al. 1992; Canfield et al. 1996; Moore et al. 2010; Sterling et al. 2015; Pariat et al. 2015), almost all have magnetic reconnections, especially the interchange reconnection between open and closed magnetic field lines, involved as the triggering mechanism of large-scale jets. In addition, they have been widely found to be related to many phenomena at different scales, including rotational motions (e.g., Liu et al. 2014; Raouafi et al. 2016; Shen 2021), waves/instabilities (e.g., Giannios & Spruit 2006; Cirtain et al. 2007; Kuridze et al. 2016; Bogdanova et al. 2018; Zhao et al. 2018; Li et al. 2023), blobs (e.g., Zhang & Ji 2014; Ni et al. 2017; Chen et al. 2022), radio bursts (e.g., Mulay et al. 2016; Hou et al. 2023), "switchbacks" in the solar wind (e.g., Sterling & Moore 2020; Raouafi et al. 2023), and coronal mass ejections (CMEs; e.g., Shen et al. 2012; Liu et al. 2015b; Zheng et al. 2016; Chen et al. 2021). These have made solar jets one of the most important phenomena that connect small and large scales, lower and higher layers, and flows and waves in the highly magnetized and stratified solar atmosphere.

Owing to their complex observational features and abundant nature, it has been rare to study the statistical and long-term behavior of solar jets using a data set with a large number of events although we have now entered an era with a tremendous amount of high spatial and high temporal resolution observations of the Sun. Musset et al. (2024) started a citizen science initiative called "Solar Jet Hunter" to utilize human resources worldwide in manually identifying coronal jets observed in the Atmospheric Imaging Assembly (AIA; Lemen et al. 2012) 304 Å passband on board the Solar Dynamics Observatory (SDO; Pesnell et al. 2012). Although more than 800 coronal jets have been reported, this approach suffers from some shortcomings, including the low efficiency of manual identification and the inconsistency of the criteria between different individuals, where the latter could pose unknown bias when statistical analysis is performed.

To facilitate more systematic studies of off-limb coronal jets with less human biases, Liu et al. (2023) developed a semiautomated jet identification algorithm (SAJIA) based on applying traditional computer vision techniques to SDO/AIA 304 Å observations. More than 1200 coronal jets were detected by applying SAJIA to SDO/AIA 304 Å observations obtained from 2010 to 2020. A power-law distribution of the jets' thermal energy was found to be highly consistent with those of microflares, indicating that they should result from the same nonlinear statistics of scale-free processes. This result was also supported by the first coronal jet butterfly diagram, which is usually seen in the migration of sunspots during solar activity cycles. By doubling the number of observations and extending them to the end of 2021, Soós et al. (2024) expanded the data set to more than 2700 coronal jets and found some intriguing oscillatory behaviors from their spatial-temporal distributions. It is worth noting that many of these detected jets are in polar regions. Previous studies suggest that solar jets at various scales (e.g., Chandrashekhar et al. 2014; Chitta et al. 2023; Uritsky et al. 2023) could contribute to energizing the solar wind. The above data set would enable further such studies from a statistical perspective.

However, it should be noted that the automated identification part in SAJIA has a relatively low precision ($\sim$0.34) and suffers from the CCD degradation of the AIA instrument (Dos Santos et al. 2021; Liu et al. 2023; Soós et al. 2024). A way to address the above issue was to check the identification results manually to eliminate fake jets. The above process was time consuming and prevented SAJIA from being deployed for real-time jet detection. This paper presents the automated jet identification algorithm (AJIA) with the U-NET neural network (Ronneberger et al. 2015). We demonstrate that the average precision of AJIA is above 0.8, which enables a more accurate coronal jet detection. The paper is organized as follows: the data set is described in Section 2, with the model and training process detailed in Section 3. Results are presented in Section 4, before the conclusions and discussions in Section 5.

2. Data

True and fake jets detected by SAJIA are used as the input of the U-NET model to be detailed in Section 3. The method of SAJIA (Liu et al. 2023) is briefly recapped as follows:

1. For a given SDO/AIA 304 Å image, a background is constructed using four images obtained on the same day and then subtracted from the given image.
2. The solar disk (with a radius of 1.02 $R_\odot$) of the background-removed image is masked as we only detect off-limb jets.
3. The masked image (4096×4096 pix^2) is downgraded to 512×512 pix^2 to reduce the computational power needed.
4. The downgraded image is then normalized and binarized with given thresholds.
5. The Douglas–Peucker algorithm (Douglas & Peucker 1973) is employed to determine the shape of bright features in the image and yield candidate polygons.
6. Polygons with four edges, inclination angles less than $60°$ and aspect ratios greater than 1.5 are kept as jet candidates.
7. Each candidate is manually checked to determine whether it is a true or fake jet.

By applying the above processes to SDO/AIA 304 Å observations from 2010 June 1 to 2021 December 31 with six images per day at a cadence of 3 hr from 00 UT, 7890 jet candidates were detected (Liu et al. 2023; Soós et al. 2024). Among all the candidates, 2704 are found to be true jets, and 5186 are fake ones, resulting in a precision of 2704/7890 $\approx$ 0.34. Initially, full-disk images that contain the above jet candidates were used to build the input of the U-NET model. However, it resulted in poor performance, with the model generating all off-limb bright features but not focusing on jets. This result was unsurprising as jets are relatively small in the full-disk observations, and other bright features would have introduced many distractions to the neural network model.

Considering that the largest detected jet has a length of approximately 70 pixels, small patches of 96×96 pix^2 centered at each jet candidate are then extracted from the masked observations (see the first three steps in SAJIA described above). This particular size of patches could minimize the appearance of nonjet features in the images while ensuring that one single jet would not be cut into several patches. These patches are then normalized to [0, 1] with a threshold of 5, which was determined via trial and error. Some examples of these patches are shown in column (a) in Figure 1, where the first three rows are true jets, and the last two contain fake jets. Patches with the same size are generated to serve as the ground truth (labels) of the neural network, with pixels covered by true jets set to 1 and all other pixels set to 0. Panels in column (b) in Figure 1 show the ground truth of the corresponding observations in panel (a). SAJIA detections are depicted in panels in column (c).

The resulting data set contains 2704 (5186) pairs of image and label patches of true (fake) jets. These true jets have projected lengths in the plane of the sky from more than 10 Mm to about 330 Mm. All jets are divided into two parts: 80% into the train set and 20% into the validation set. However, the data set is imbalanced as there are 91.7% more fake jets than true jets. To solve this problem, new images and labels are generated by randomly flipping and rotating (between $\pm 0.4\pi$, big enough to introduce differences between the original and created images, while still less than 0.5π above which many parts of the images would be cropped) the original images and labels of true jets. The above data augmentation is performed separately in the train and test sets to avoid possible data
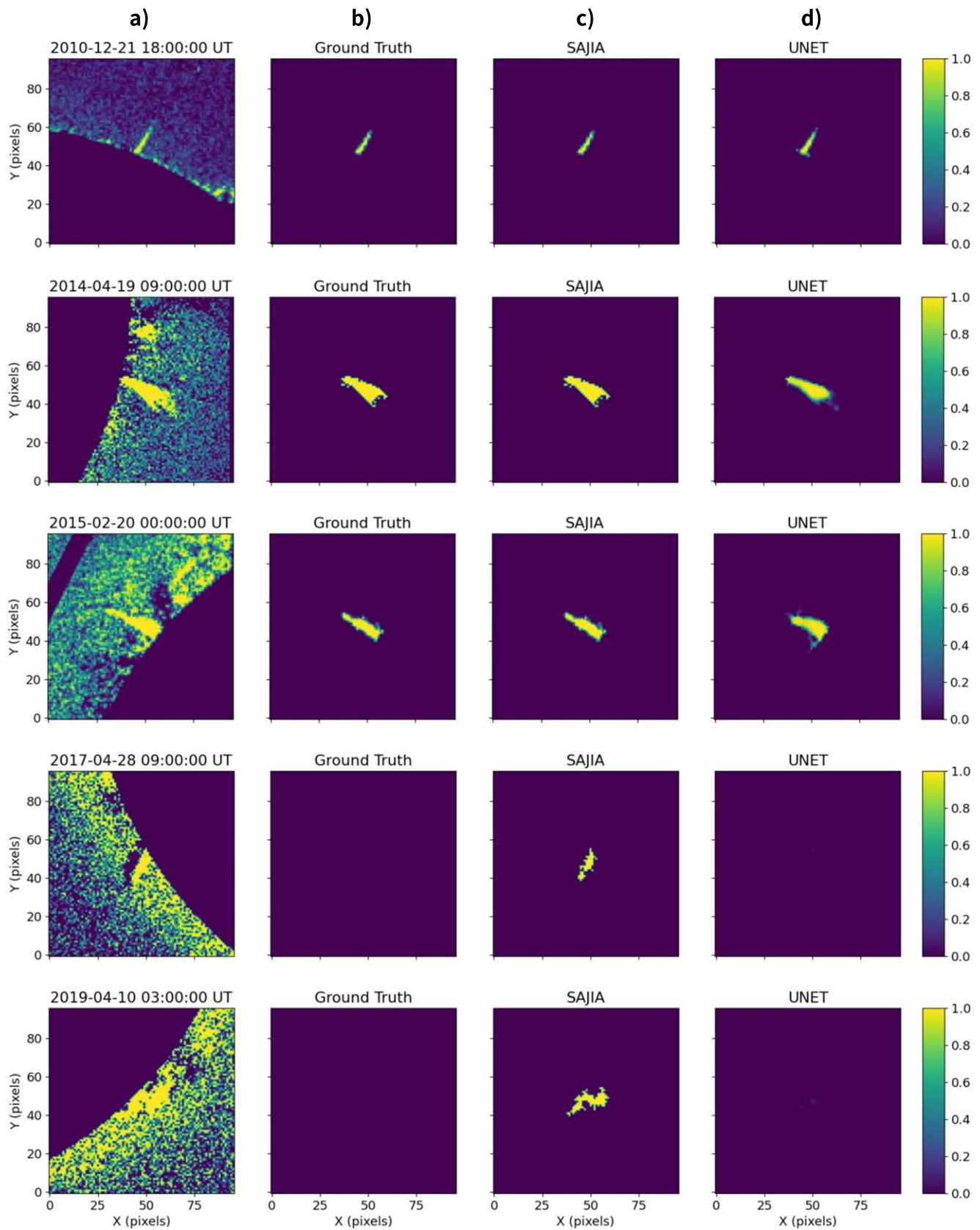
Figure 1. Examples of coronal jets and detection results. Images in column (a) are patches of SDO/AIA 304 Å observations with a size of 96×96 pix^2. Column (b) lists the corresponding ground truths where yellow colors denote pixels belonging to jets. Column (c) shows detection results by the SAJIA developed by Liu et al. (2023). Panels in column (d) are the jet detection results by the AJIA proposed in this paper.
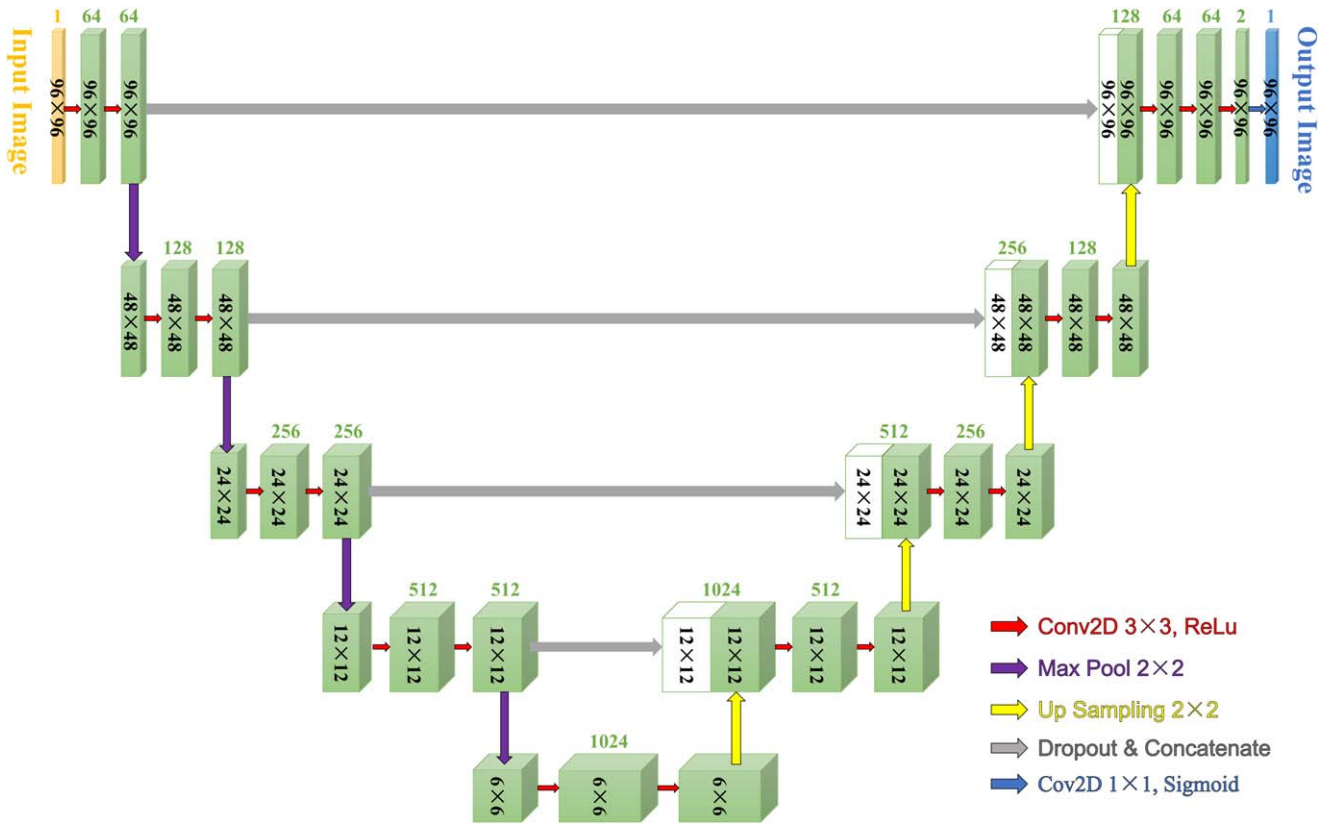
Figure 2. Architecture of U-NET. This cartoon is adopted from Ronneberger et al. (2015). See Section 3 for a detailed description of the U-NET architecture.

leakage. After the data augmentation, the data set is balanced with 5186 fake jets and 5408 true jets. The final data set has 8474 (2120) pairs of images and labels in the train (test) set.

3. Model and Training

The U-NET convolutional neural network architecture (see Figure 2) was initially proposed by Ronneberger et al. (2015) for biomedical image segmentation purposes. It was applied to transmitted-light microscopy images and won the ISBI Cell Tracking Challenge 2015 (Ronneberger et al. 2015). U-NET was then modified and successfully applied for different kinds of image segmentation purposes, including 3D image segmentation and road segmentation (e.g., Minaee et al. 2021).

U-NET contains several convolutional layers with different filter sizes. In the first step, the input image with a size of $96 \times 96 \times 1$ (yellow block in Figure 2) is taken into two convolutional layers, each having 64 filters with a kernel size of 3×3. In each layer, the rectified linear unit activation function is used after each convolutional operation, where $\text{ReLU}(x) = \max(0, x)$. The resulting image after the first step has a size of $96 \times 96 \times 64$. This image is then downsampled to $48 \times 48 \times 64$ by a max pooling operation (purple arrows in Figure 2), where only the maximum value in every 2×2 region in the image is kept and all other pixels are discarded. The image is then taken into the next step, which contains two convolutional layers but doubles the number of filters (128).

The above process is repeated until the image size is downsampled to 6×6 but with 1024 filters. Then, a reverse series of operations of the above process is performed to upsample (yellow arrows in Figure 2) the image until it again has a size of $96 \times 96 \times 64$. Two extra convolutional layers with

2 and 1 filters are used to generate the final output image (blue block in Figure 2). This unique convolutional neural network is named "U-NET" as its architecture resembles the letter U (Figure 2). The left (right) part of U-NET is usually called the encoder (decoder). Layers in the encoder are skip connected with layers in the decoder (gray arrows in Figure 2). These skip connections remind U-NET of the fine details learned in the encoder that could be used to construct images in the decoder. It has been found particularly effective and successful in image segmentation as its contracting path (downsampling) can capture the context of an image, and its symmetric expanding path (upsampling) can enable precise localization (Ronneberger et al. 2015). The loss function of U-NET is set to be the binary cross-entropy loss, which is defined as follows:

$$\log(L) = \frac{1}{N}\sum_{i=1}^{N}[y_i \log(\hat{y}_i) + (1 - y_i)\log(1 - \hat{y}_i)], \qquad (1)$$

where L is the loss. N is the number of pixels in each image. y_i is the value (0 or 1) of each pixel in the label, and $\hat{y}_i$ is the corresponding prediction value (0 to 1).

All 8474 pairs of images and labels in the train set were taken into the above U-NET neural network to train a jet identification model. Considering the capacity of the GPU (Nvidia GeForce GTX 4090 with a RAM of 24 GB), the batch size was set to be 256. Another vital hyperparameter during training is the learning rate. The learning rate determines how much the model weights are updated in response to the loss of each batch. A too-big learning rate will result in the model skipping the minimum of the loss function and making it hard to converge, while a too-small learning rate will probably trap the model in a local minimum of the loss function. A common
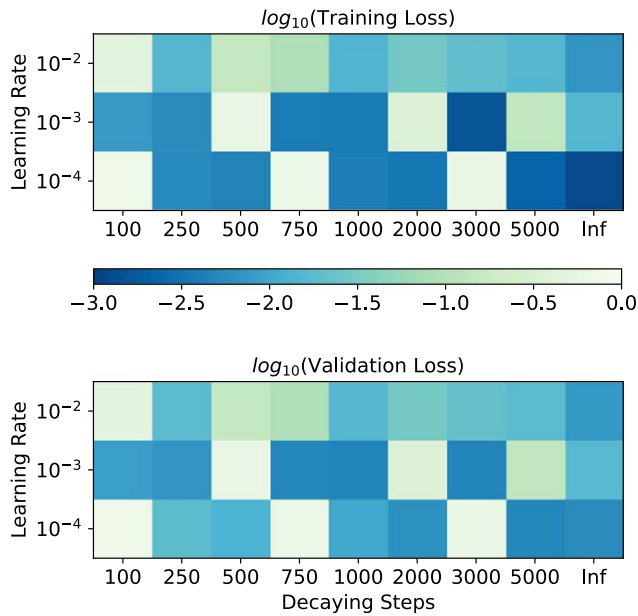
Figure 3. Model losses under different learning rates. The upper (lower) panel shows the logarithm of the training (validation) losses for different combinations of learning rates and decaying steps. A decaying step of Inf means the learning rate is fixed without any decaying.

practice is to set a relatively large learning rate at the beginning of the training and decrease it along a given function at certain steps. In the case of our model, a cosine decay function is used to prevent the learning rate from decreasing too fast (see, e.g., Loshchilov & Hutter 2016, for more details).

Figure 3 depicts the losses obtained in the train (upper panel) and validation sets (lower panel) with different initial learning rates and decaying steps. An "infinite" decaying step represents a fixed learning rate without decay during training. It can be seen from Figure 3 that the minimum losses (in the order of $\sim 10^{-3}$) in both the train and validation sets can be achieved when the learning rate is fixed at 10^{-4}.

4. Results

4.1. Model selection

The blue curve in Figure 4 is the evolution of the training loss, with a fixed learning rate of 10^{-4}. It is seen that the training loss decreases as the number of training epochs grows and reaches its minimum of 1.2×10^{-3} at 117 epochs. At 117 epochs, the validation loss (orange curve in Figure 4) is 5.5×10^{-3}, which is also around its minimum. Two other commonly used parameters to measure the performance of image segmentation tasks are the mean average precision (mAP) and the mean intersection over union (mIoU). Here, we report that, at 117 epochs, the trained model has an mAP of 0.87 and an mIoU of 0.50 for the training set and an mAP of 0.58 and an mIoU of 0.50 for the validation set.

Based on the above observations, we use the model trained at 117 epochs as the final coronal jet identification model. This model could take the 96×96 patches of the SDO/AIA 304 Å observations as its input and automatically identify coronal jets (thus named AJIA). Images in column (d) in Figure 1 are the predictions by AJIA based on the inputs in column (a). Colors in the images denote the possibility of the corresponding pixels belonging to jets. A pixel with a value of 1 (0) means that AJIA thinks there is a 100% (0%) chance that this pixel belongs to a
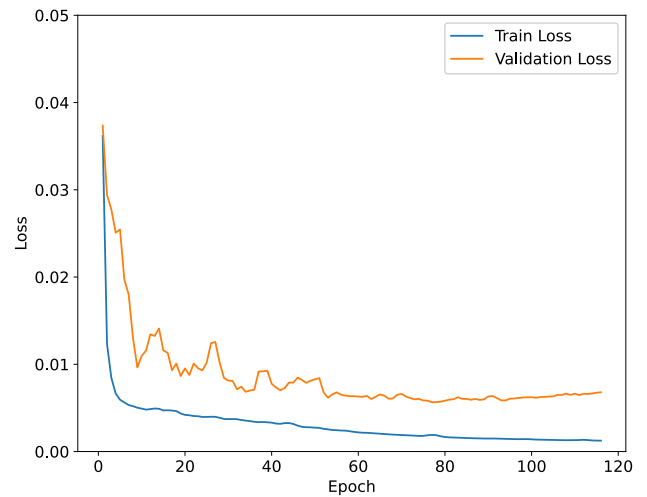

Figure 4. Training history with a fixed learning rate of 10^{-4}. The blue (orange) curve is the evolution of the training (validation) loss.

jet. In the first three rows, where true jets are present in the input images, AJIA could successfully identify jets almost identical to the ground truths. In the last two rows, where there are no jets but our traditional jet identification algorithm SAJIA (Liu et al. 2023) wrongly detects jets, AJIA successfully avoids making the same mistakes.

4.2. Model Evaluation

To evaluate the performance of AJIA, a threshold needs to be defined—only above which the detected feature by AJIA can be considered a jet. For example, if we have a threshold of T, a detected feature by AJIA can be considered a jet (true/positive) only if the maximum predicted value of the feature by AJIA is no less than T. Otherwise, it is considered as nonjet (fake/negative). Panel (a) in Figure 5 shows how the recall, the true negative rate (TNR), the precision, and the F-measure evolve with different thresholds T. Recall, TNR, precision, and F-measure are defined as follows:

$$\text{Recall} = \frac{\text{TP}}{\text{TP} + \text{FN}},$$

$$\text{TNR} = \frac{\text{TN}}{\text{TN} + \text{FP}},$$

$$\text{Precision} = \frac{\text{TP}}{\text{TP} + \text{FP}},$$

$$\text{F} - \text{Measure} = \frac{2 * \text{Precision} * \text{Recall}}{\text{Precision} + \text{Recall}}, \quad (2)$$

where TP is true positive (AJIA successfully detects the jet in the label), FN is false negative (AJIA misses the jet in the label), TN is true negative (there is no jet in the label, and AJIA also does not detect any jet), and FP is false positive (there is no jet in the label but AJIA detects a jet). One can see from the above definitions that recall represents the percentage of true jets in the labels that are successfully detected by AJIA. TNR denotes the percentage of fake jets in the labels that are also considered fake jets by AJIA. Precision is the percentage of true jets in all jets detected by AJIA. F-measure measures the combined effect of precision and recall.

We can see from Figure 5(a) that both TNR and precision increase as the threshold grows. However, the recall decreases
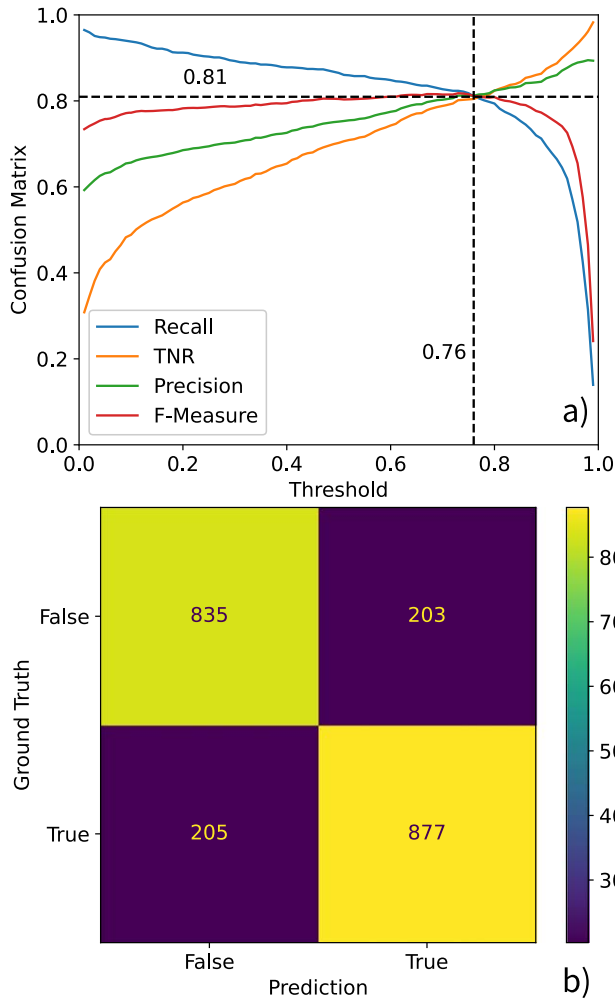
Figure 5. Confusion matrix of the trained U-NET model. Panel (a) shows how the recall (blue curve), TNR (orange curve), precision (green curve), and F-measure (red curve) changes with different thresholds. See Equation (1) for the definitions of the above measurements. Panel (b) is the distribution of true and fake jets in the input labels and predictions made by AJIA.

Figure 6. Confusion matrix of AJIA with 1 hr cadence data. Similar to panel (b) in Figure 5, this figure shows the distribution of true and fake jets in the input labels and predictions made by AJIA from the 235 true and 174 fake jets detected in 2011 January.

with the threshold. When the threshold is around 0.76, the F-measure peaks at ∼0.81, and all three other measurements converge at similar values. This suggests that a threshold of 0.76 would give the most ideal and balanced performance. Figure 5(b) is a comparison between the ground truths and the predictions of AJIA. Among 1040 candidates identified by AJIA, 835 (205) are true (fake) jets, yielding a precision of ∼80.3%.

4.3. Application to Higher-cadence Data

The current data set used for building the model was generated by Liu et al. (2023) and Soós et al. (2024) and contains coronal jets detected with a cadence of 3 hr. This low cadence, together with the relatively low precision of SAJIA, results in a missing rate of ∼30% in nonpolar regions (see estimations in Liu et al. 2023) and prevents us from further studying the temporal evolution of the detected jets. The high performance of AJIA indicated by its high recall, TNR, precision, and F-measure, as detailed in the previous subsection, provides an excellent opportunity to look into the above issue via automatically detecting jets with high accuracy at higher cadences.
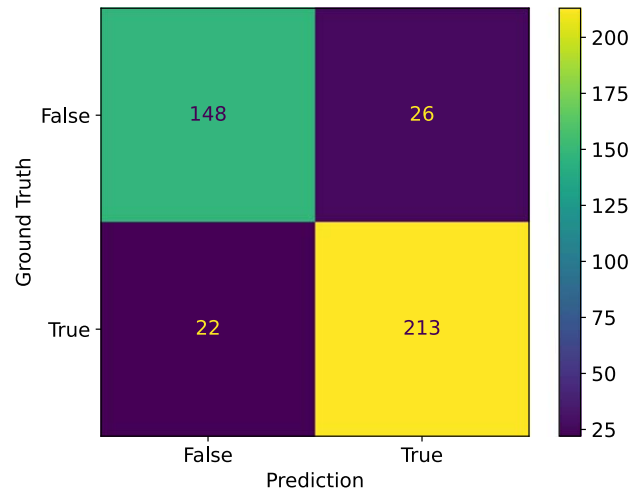
To test the application of AJIA to higher-cadence data, we employed SAJIA to detect coronal jets at 1 hr intervals from 00:30 UT every day throughout 2011 January. SAJIA yields 409 jet candidates, compared to 68 jet candidates given by SAJIA with a 3 hr cadence in 2011 January. After laborious identification of these jet candidates by downloading and checking their temporal evolution one by one, 235 are identified as true, and the other 174 are fake. Among all fake jets, ∼94% are (part of) prominences, CMEs, or coronal rains. This gives a precision of SAJIA of ∼51%, consistent with the findings in Liu et al. (2023) and Soós et al. (2024; also see discussions in Section 5).

These jets were not included in the previous data set employed to build AJIA and could be used to test the application of AJIA to unknown events. Figure 6 depicts the confusion matrix of AJIA's prediction on the above 235 true and 174 fake jets. TP, TN, FP, and FP are 213, 148, 26, and 22, respectively. This indicates that the precision of AJIA in detecting these unknown events is about 0.81. The recall, TNR, and F-measure are 0.81, 0.80, and 0.81, respectively. These values are consistent with what was found in the validation set as described in the previous subsections and further suggest AJIA's potential to detect off-limb coronal jets accurately.

5. Conclusions and Discussions

In this paper, we presented the development of the Automated Jet Identification Algorithm (AJIA), which is built based on off-limb coronal jets detected by our previously developed semiautomated jet identification algorithm (SAJIA; Liu et al. 2023). These jets were fed into a U-NET (Ronneberger et al. 2015) neural network to train the final model. Evaluating AJIA on a test set containing 2120 true and fake jets yields a precision, recall, TNR, and F-measure of around 0.81, where the precision is significantly larger than that of SAJIA (0.34).

It was found in Soós et al. (2024) that the precision of SAJIA is heavily impacted by the CCD degradation of SDO/AIA. Diamonds connected by dashed lines in Figure 7 are the precisions of SAJIA measured each year (inferred from Table 1 in Soós et al. 2024), with colors denoting the normalized
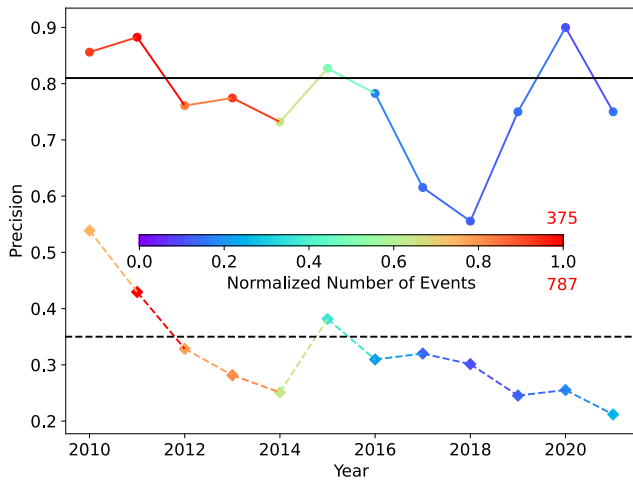
Figure 7. Precision of AJIA and SAJIA for jets in different years. Colored dots and the solid curve are the yearly precisions of AJIA, with colors denoting the normalized (to the red number 375) number of events. Colored diamonds and the dashed curve are the yearly precisions of SAJIA, with colors denoting the normalized (to the red number 787) number of events, using data from Soós et al. (2024).

number of events. In general, the precision of SAJIA undergoes an overall decreasing trend, which is consistent with the overall decreasing sensitivity of the SDO/AIA detectors (e.g., Dos Santos et al. 2021). We demonstrate that AJIA is not affected by the same effect although it was trained using SDO/AIA 304 Å images before being corrected for CCD degradation. Dots connected by solid lines in Figure 7 are the precisions of AJIA measured each year, where colors are the normalized number of events. It can be seen that the performance of AJIA does not decrease with time, and its minimum value (>0.55 in 2018) is above the maximum precision of SAJIA ($\sim$0.54 in 2010).

To conclude, AJIA is a step forward compared to SAJIA as it is more precise (with a precision of 0.81) and not affected by CCD degradation. AJIA is also fast, and it takes less than 6 s to make predictions for all 2120 images in the test set (2.6 ms per image). Another advantage of AJIA should be noted—it gives the "possibility" of whether a pixel in the observation belongs to a jet or not (see column (c) in Figure 1). This enables us to generate jet heat maps directly from SDO/AIA 304 Å observations and allows real-time jet detection and visualization. These advantages of AJIA are essential in enabling many pieces of research, including, but not limited to, studying the collective behavior of coronal jets over the long term, their evolution over the solar activity cycles, and their relation with other solar phenomena (see, e.g., Liu et al. 2023; Soós et al. 2024).

Future work will also focus on improving AJIA's detection precision, which might be achieved by adding several fully connected layers after U-NET instead of giving a fixed threshold, as was done in this work. Another future work will utilize the improved model to detect more jets at a much higher cadence (i.e., 1 hr or less) than 3 hr to explore the temporal aspects of coronal jets, especially given the capability of AJIA in accurately detecting jets from such data as described in Section 4.3. This will also enable the study of their velocities by developing a dedicated automated algorithm using techniques, including, but not limited to, the surfing transform technique (Uritsky et al. 2023), the Gaussian fitting method (Chitta et al. 2023), and the optical flow estimation

(Fleet & Weiss 2006). Their kinetic energy would further be estimated, and the existence of a power-law distribution, which is essential in understanding the fundamental physics of the release of free magnetic energy in the solar atmosphere, would then be examined following Liu et al. (2023) and Uritsky et al. (2023).

This will further enable a series of statistical studies that were not done before due to the relatively small number of events detected. For example, Liu et al. (2023) found the "butterfly diagram" of coronal jets where the average latitudes of jets migrate from mid-latitudes to the equator from the beginning to the end of the solar activity cycle. It is well known that magnetic elements in high latitudes also migrate toward the polar regions throughout the solar cycle. However, this trend was not seen in Liu et al. (2023), and whether its absence is caused by the limited number of events or the possibly different triggering mechanisms between jets originating from active regions and nonactive regions is yet to be examined by building a larger data set with more events.

By having more samples of off-limb coronal jets, the distributions and differences of active-region, quiet-region, and polar jets can be further studied. Their different behaviors during solar activity can also be evaluated. The future large data set would also enable statistical studies on how coronal jets can gain their kinetic energy (e.g., Liu et al. 2014), how many twists they release (e.g., Liu et al. 2019c), and how the magnetic energy is distributed to different forms of energies during their eruption (e.g., Liu et al. 2016). Moreover, preliminary evidence of the so-called solar active longitude (e.g., Gyenge et al. 2017) was given in both Liu et al. (2023) and Soós et al. (2024), but more evidence can be supplied by studying a significantly larger number of jets. Finding and validating active longitudes from these small-scale events will be significant for the theory and simulation of the solar dynamo.

ORCID iDs

Jiajia Liu (刘佳佳) ⓘ https://orcid.org/0000-0003-2569-1840
Chunyu Ji (季春瑜) ⓘ https://orcid.org/0009-0006-4430-7882
Yimin Wang (王宜敏) ⓘ https://orcid.org/0000-0002-8835-3825
Szabolcs Soós ⓘ https://orcid.org/0000-0002-3606-161X
Ye Jiang (姜也) ⓘ https://orcid.org/0000-0002-6683-0205
Robertus Erdélyi ⓘ https://orcid.org/0000-0003-3439-4127
M. B. Korsós ⓘ https://orcid.org/0000-0002-0049-4798
Yuming Wang (汪毓明) ⓘ https://orcid.org/0000-0002-8887-3919

References

Battaglia, A. F., Canivete Cuissa, J. R., Calvo, F., Bossart, A. A., & Steiner, O. 2021, A&A, 649, A121
Beckers, J. M. 1968, SoPh, 3, 367
Bogdanova, M., Zhelyazkov, I., Joshi, R., & Chandra, R. 2018, NewA, 63, 75
Brooks, D. H., Kurokawa, H., & Berger, T. E. 2007, ApJ, 656, 1197
Canfield, R. C., Reardon, K. P., Leka, K. D., et al. 1996, ApJ, 464, 1016
Chandrashekhar, K., Bemporad, A., Banerjee, D., Gupta, G. R., & Teriaca, L. 2014, A&A, 561, A104
Chen, H., Yang, J., Hong, J., Li, H., & Duan, Y. 2021, ApJ, 911, 33
Chen, J., Erdélyi, R., Liu, J., et al. 2022, FrASS, 8, 1
Chen, J., Su, J., Deng, Y., & Priest, E. R. 2017, ApJ, 840, 54
Chitta, L. P., Zhukov, A. N., Berghmans, D., et al. 2023, Sci, 381, 867
Cirtain, J. W., Golub, L., Lundquist, L., et al. 2007, Sci, 318, 1580
De Pontieu, B., McIntosh, S., Hansteen, V. H., et al. 2007, PASJ, 59, 655
Dey, S., Chatterjee, P., O. V. S. N., M., et al. 2022, NatPh, 18, 595
Dos Santos, L. F. G., Bose, S., Salvatelli, V., et al. 2021, A&A, 648, A53
Douglas, D. H., & Peucker, T. K. 1973, Cartographica, 10, 112
Filippov, B., Koutchmy, S. L., & Tavabi, E. 2011, SoPh, 286, 143
Fleet, D., & Weiss, Y. 2006, in Optical Flow Estimation, ed. N. Paragios, Y. Chen, & O. Faugeras (Berlin: Springer), 237
Giannios, D., & Spruit, H. C. 2006, A&A, 450, 887
Goodman, M. L. 2012, ApJ, 757, 188
Gyenge, N., Singh, T., Kiss, T. S., Srivastava, A. K., & Erdélyi, R. 2017, ApJ, 838, 18
He, J., Marsch, E., Tu, C., & Tian, H. 2009, ApJ, 705, L217
Heggland, L., De Pontieu, B., & Hansteen, V. H. 2007, ApJ, 666, 1277
Hou, Z., Tian, H., Su, W., et al. 2023, ApJ, 953, 171
Jess, D. B., Mathioudakis, M., Erdélyi, R., et al. 2009, Sci, 323, 1582
Jess, D. B., Pascoe, D. J., Christian, D. J., et al. 2012, ApJ, 744, L5

Kudriavtseva, A. V., & Prosovetsky, D. V. 2019, JASTP, 193, 105039
Kuridze, D., Zaqarashvili, T. V., Henriques, V., et al. 2016, ApJ, 830, 133
Lemen, J. R., Title, A. M., Akin, D. J., et al. 2012, SoPh, 275, 17
Li, X., Keppens, R., & Zhou, Y. 2023, ApJL, 947, L17
Liu, J., Fang, F., Wang, Y., et al. 2015a, AGUFM, 2015 SH31B–2405
Liu, J., Nelson, C. J., & Erdélyi, R. 2019a, ApJ, 872, 22
Liu, J., Nelson, C. J., Snow, B., Wang, Y., & Erdélyi, R. 2019b, NatCo, 10, 3504
Liu, J., Song, A., Jess, D. B., et al. 2023, ApJS, 266, 17
Liu, J., Wang, Y., Erdélyi, R., et al. 2016, ApJ, 833, 150
Liu, J., Wang, Y., & Erdélyi, R. 2019c, FrASS, 6, 44
Liu, J., Wang, Y., Liu, R., et al. 2014, ApJ, 782, 94
Liu, J., Wang, Y., Shen, C., et al. 2015b, ApJ, 813, 115
Loshchilov, I., & Hutter, F. 2016, arXiv:1608.03983
Minaee, S., Boykov, Y. Y., Porikli, F., et al. 2021, ITPAM, 44, 3523
Moore, R. L., Cirtain, J. W., Sterling, A. C., & Falconer, D. A. 2010, ApJ, 720, 757
Moore, R. L., Sterling, A. C., Cirtain, J. W., & Falconer, D. A. 2011, AJ, 731, L18
Mulay, S. M., Tripathi, D., Zanna, G. D., & Mason, H. 2016, A&A, 589, A79
Musset, S., Jol, P., Sankar, R., et al. 2024, A&A, 688, A127
Newton, H. W. 1934, MNRAS, 94, 472
Ni, L., Zhang, Q.-M., Murphy, N. A., & Lin, J. 2017, ApJ, 841, 27
Oxley, W., Scalisi, J., Ruderman, M. S., & Erdélyi, R. 2020, ApJ, 905, 168
Pariat, E., Dalmasse, K., DeVore, C. R., Antiochos, S. K., & Karpen, J. T. 2015, A&A, 573, 539
Pesnell, W. D., Thompson, B. J., & Chamberlin, P. C. 2012, SoPh, 275, 3
Raouafi, N. E., Patsourakos, S., Pariat, E., et al. 2016, SSRv, 201, 1
Raouafi, N. E., Stenborg, G., Seaton, D. B., et al. 2023, ApJ, 945, 28
Ronneberger, O., Fischer, P., & Brox, T. 2015, arXiv:1505.04597
Samanta, T., Tian, H., Yurchyshyn, V., et al. 2019, Sci, 366, 890
Scalisi, J., Oxley, W., Ruderman, M. S., & Erdélyi, R. 2021a, ApJ, 911, 39
Scalisi, J., Ruderman, M. S., & Erdélyi, R. 2021b, ApJ, 922, 118
Schmieder, B., Joshi, R., & Chandra, R. 2022, AdSpR, 70, 1580
Sekse, D. H., van der Voort, L. R., & Pontieu, B. D. 2012, AJ, 752, 108
Shen, Y. 2021, RSPSA, 477, 217
Shen, Y., Liu, Y., Su, J., & Deng, Y. 2012, ApJ, 745, 164
Shibata, K., Ishido, Y., Acton, L. W., et al. 1992, PASJ, 44, L173
Soós, S., Liu, J., Korsós, M. B., & Erdélyi, R. 2024, ApJ, 965, 43
Sterling, A. C. 2000, SoPh, 196, 79
Sterling, A. C., & Moore, R. L. 2020, ApJ, 896, L18
Sterling, A. C., Moore, R. L., Falconer, D. A., & Adams, M. 2015, Natur, 523, 437
Uritsky, V. M., Karpen, J. T., Raouafi, N. E., et al. 2023, ApJL, 955, L38
Zhang, Q. M., Huang, Z. H., Hou, Y. J., et al. 2021, A&A, 647, A113
Zhang, Q. M., & Ji, H. S. 2014, A&A, 567, A11
Zhao, T., Ni, L., Lin, J., & Ziegler, U. 2018, RAA, 18, 45
Zhelyazkov, I., Zaqarashvili, T. V., Chandra, R., Srivastava, A. K., & Mishonov, T. 2015, AdSpR, 56, 2727
Zheng, R., Chen, Y., Du, G., & Li, C. 2016, AJ, 819, L18